Check for updates

Received: 11 December 2021 | Revised: 12 March 2022 | Accepted: 21 March 2022

DOI: 10.1002/jbio.202100379

RESEARCH ARTICLE

JOURNAL OF BIOPHOTONICS

Noises investigations and image denoising in femtosecond stimulated Raman scattering microscopy

Rajeev Ranjan[1,2] | **Giovanni Costa**[1,3] | **Maria Antonietta Ferrara**[1] | **Mario Sansone**[3] | **Luigi Sirleto**[1*]

[1]National Research Council (CNR), Institute of Applied Sciences and Intelligent Systems, Napoli, Italy

[2]Department of Biochemistry and Molecular Pharmacology, New York University School of Medicine, New York, New York, USA

[3]Department of Electrical Engineering and Information Technologies (DIETI), University "Federico II" of Naples, Naples, Italy

***Correspondence**
Luigi Sirleto, National Research Council (CNR), Institute of Applied Sciences and Intelligent Systems, Napoli, Italy.
Email: luigi.sirleto@cnr.it

Abstract

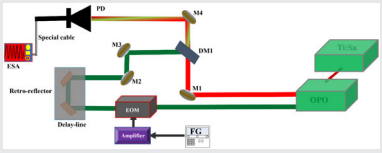

In the literature of SRS microscopy, the hardware characterization usually remains separate from the image processing. In this article, we consider both these aspects and statistical properties analysis of image noise, which plays the vital role of joining links between them. Firstly, we perform hardware characterization by systematic measurements of noise sources, demonstrating that our *in-house built* microscope is shot noise limited. Secondly, we analyze the statistical properties of the overall image noise, and we prove that the noise distribution can be dependent on image direction, whose origin is the use of a lock-in time constant longer than pixel dwell time. Finally, we compare the performances of two widespread general algorithms, that is, singular value decomposition and discrete wavelet transform, with a method, that is, singular spectrum analysis (SSA), which has been adapted for stimulated Raman scattering images. In order to validate our algorithms, in our investigations lipids droplets have been used and we demonstrate that the adapted SSA method provides an improvement in image denoising.

KEYWORDS

microscopy, optics, Raman microscopy, relative intensity noise, stimulated Raman scattering microscopy

1 | INTRODUCTION

In nonlinear microscopy, due to many reasons, the signal obtained by nonlinear interaction is usually combined with noise. The most common types of noise are Johnson noise, shot noise in lasers/detectors and laser-intensity $1/f$ noise [1, 2]. Johnson noise is caused by the thermal agitation of electrons in a resistor, so it depends on temperature but is independent of the geometry and material of the circuit. The quantum nature of electrons and statistical fluctuations in the generated photocurrent and the dark current cause shot noise in detectors. In a laser, shot noise is caused by fundamental fluctuations in the photon stream, which constitutes the standard quantum limit. Laser-intensity $1/f$ noise is due to external influences such as mechanical vibrations, electrical

This is an open access article under the terms of the Creative Commons Attribution-NonCommercial-NoDerivs License, which permits use and distribution in any medium, provided the original work is properly cited, the use is non-commercial and no modifications or adaptations are made.
© 2022 The Authors. *Journal of Biophotonics* published by Wiley-VCH GmbH.

and/or thermal noise, electromagnetic interferences and pressure fluctuations. For pulsed lasers, the excess noise contribution, due to its $1/f$ behavior, strongly depends on the laser modulation frequency. For modulation frequency, over 1 MHz, the excess noise should be negligible while the shot noise should be dominant [1].

Image denoising plays a vital role in a wide range of applications such as image restoration, visual tracking, image segmentation and image classification [3–5]. A straightforward and effective approach for denoising signals, which can be applied in many different fields, consists of averaging n acquisitions of the same sample, being the noise additive and stationery. The signal to noise ratio (SNR) is improved by a factor of $\sqrt{n}$ with respect to a single acquisition, but acquisition time increases, as multiple acquisitions are required. One of the main limitations of this approach is that it cannot be applied to a fundamental class of biomedical imaging experiments, that is, in-vivo applications. Indeed, in such an experiment, to avoid imaging artifacts, a fast image collection is required due to the motion of the specimen during acquisition.

The most popular and well-established denoising algorithms are based on spectral analysis, principal component analysis and singular value decomposition [6]. Another powerful tool, which has been commonly used over the past decade, is discrete wavelet transform (DWT). Compared to the more traditional Fast Fourier Transform, the DWT has many advantages: edge preservation, flexibility to adapt to specific denoising problems and a very low computational cost [7]. In recent years, there has been an increasing interest in convolutional neural networks (CNNs) also in biophotonics and imaging communities [8]. However, the complexity of the reported noise reduction algorithms could limit their broad applications due to the need to pre-prepare plenty of images for learning and complex parameter adjustment for different experiments.

Stimulated Raman scattering (SRS) microscopy enables imaging systems, performing label-free imaging with high sensitivity, high spatial and spectral resolution, 3D sectioning and fast image acquisition [9–12]. In SRS microscopy, in order to obtain images, two synchronized and collinear laser pulsed beams called pump and Stokes signals, with independent tunability over a wide spectral range, are required. When their difference in energy is equal to vibrational energy (ω_v) of the sample, an exchange of energy between the two beams can occur, and a gain in the Stokes signal (stimulated Raman gain) and a loss in the pump signal (stimulated Raman loss) can be obtained. In SRS, a slight variation in an intense laser beam (the transmitted probe or pump) on the scale of 10^{-5} to 10^{-4} has to be detected, which can be contaminated by laser intensity noise. Since, the SRS output signal and excitation pulses have the same wavelengths, their spectral separation is impossible, so most SRS studies take advantage of high-frequency optical modulation and phase-sensitive detection. An electro-optic modulator (EOM) applies a high-frequency modulation to one pulse train, and the modulation is transferred to the other beam. After removing the modulated beam by a stack of optical filters, the probe beam is detected by a photodetector (PD). Its output is routed through a low pass filter to a lock-in amplifier (LIA), in which the large DC background is filtered out, while the small modulation due to the SRS signal is measured. We note that taking advantage of a high-frequency modulation scheme (faster than 1 MHz), the laser relative intensity noise (RIN) can be reduced to the level of shot noise while using sufficiently high laser powers, the shot-noise can surpass the thermal noise. Definitely, combining the two conditions: a high-frequency modulation scheme and moderate laser powers, shot-noise limited detection can be achieved. Nevertheless, due to the weak Raman cross-section of biomolecules, SRS images often suffer from low SNR, so SRS applications in biological/biomedical imaging can be compromised [13–24].

In the literature of SRS, great attention is given to technological and application advances, while the investigations of noise are often overlooked, although SNR is a crucial issue not only for biological imaging, but also for spectroscopic applications [25, 26]. The hardware characterizations, usually, are carried out to assess the shot noise condition [27–32]. A systematic study of SRS noise was reported in ref. [29], in which the optimization of the ultimate SRS detection limit in a conventional lock-in-based SRS system was investigated. Concerning image processing, it is mainly devoted to denoising signals [33–37]. However, the link between hardware characterization and imaging processing often is not highlighted. As an established practice, in order to justify the hypothesis of white noise, generally supposed by many algorithms, the condition of shot noise limited obtained by hardware characterization is considered enough.

It is worth noting that an appropriate application of denoising algorithms typically requires knowledge about the interfering noise. Therefore, the statistical properties of the overall image noise, allowing to adapt denoising algorithms to signal images, are crucial. In this article, we focus not only on hardware characterization and image processing, but also on statistical properties of the image, and we experience that the latter can join links between them.

Most denoising algorithms were designed for two dimensional (2D) images, while for higher dimensional data, for example, videos, the consistency along the third dimension is still a challenge. In Reference 33, to solve this issue in SRS imaging, a denoising algorithm, removing the

noise in both spatial and spectral domains by total variation minimization, was demonstrated. In Reference 34, a fast nonaverage denoising and high-precision Raman shift extraction method, based on a self-reinforcing SNR enhancement algorithm, was reported for SRS spectroscopy and microscopy. Recently, denoising of SRS microscopy images via deep learning was investigated [35–37]. A drawback of this approach is that the architecture of the most common CNNs for denoising involve significant training times and requires large training samples to be effective. We note that the use of complicated algorithms could not be standard in the SRS community, it could discourage the wide diffusion of SRS, and it could be a severe limitation for some applications, for example, in-vivo experiments. Definitely, the development of simple, efficient and high accuracy denoising methods is highly desirable. Therefore, in this article, aimed to avoid complicated algorithms, we explore the potentiality of some widespread general algorithms.

In this article, noise sources quantifications, statistical properties analysis of image noise and image denoising in SRS microscopy are reported.

Noises quantifications were performed in two steps. In the former, being the SRS sensitivity inversely related to the RINs of laser beams [29], RIN measurements on 2 femtosecond laser sources (Ti:Sa and OPO) were carried out. In the latter, noises in the detection system were investigated. Since in a LIA the noise in the input signal near the reference frequency appears as noise in the output signal, noise measurements as a function of laser power were carried out. We are aware that the noise characterization of laser and detection systems are obtained by standard experimental techniques. However, since our SRS microscope is a home built system we believe that a detailed description of these experiments is important to assess the achievement of shot noise limited condition. In addition, a statistical properties analysis of overall image noise was carried out, and we demonstrate that the background noise is white along the slow axis, while it is correlated along the fast axis. This is the new result and crucial point proposed by our article: even if the hardware characterization demonstrates that shot noise limited condition is achieved, we prove that the imaging system can be affected by correlated noise. Therefore, the established practice we said before is not correct. Finally, the results obtained from statistical properties analysis show that a 1D technique based on singular spectrum analysis (SSA) [38, 39] has been tailored for SRS imaging denoising. The results from SSA have been compared with two well-established and commonly applied algorithms: DWT and SVD, and a significant improvement of SNR, obtained using our adapted method, is demonstrated.

The article is organized as follows: in the second paragraph, a short description of our *in-house* built microscope is reported, and methods for noises investigations and algorithms for denoising are briefly described; afterward, in the third paragraph, results concerning noise measurements in lasers, spectroscopic setup and imaging system and image denoising are reported and discussed.

2 | EXPERIMENTAL SETUP AND METHODS

The optical architecture of our implemented SRS microscope, covering the C—H region (above 2500 cm^{-1}) of the Raman spectrum, was reported in our earlier articles [40–46]. It was briefly obtained by integrating a femtosecond stimulated Raman spectroscopy with an inverted Nikon Ti-Eclipse microscope equipped with a scan head. The spectroscopic setup was provided with two femto laser sources: a Ti:Sa (Chameleon Ultra II) and a synchronized optical parametric oscillator (Chameleon Compact OPO). The intensity modulation of Ti:Sa pulses at a frequency of 5 MHz was obtained by an EOM (350-160 KD*P CONOPTICS). The two pulsed laser beams were first overlapped in both space and time and then focused into the sample by a microscope objective (×60, NA = 1.27). Afterward, an upper objective (×40, NA = 1.25) collected the transmitted output pulses, a stack of optical filters removed pump pulses, while a photodiode detected the modulation transmitted to the probe beam. In order to extract the modulation depth, the measured signal was demodulated by a LIA (SR844-200 MHz dual phase). 2D images were realized through-beam scanning by two galvo mirrors. In Figure 1, the experimental optical architecture of our SRS microscope is reported.

2.1 | Noise measurements in laser sources

Fluctuations in laser intensity can overtake the thermal noise and/or the shot noise of the PD, becoming a limiting factor for the sensitivity of the system. RIN describes the contributions of the laser intensity fluctuations to the electrical noise in the receiver relative to the signal power observed electrically. If $\delta P(t)$ is the output power fluctuation and $<P>$ the average value, the intensity autocorrelation function is given by:

$$C_{pp}(\tau) = \frac{\langle \delta P(t) \delta P(t+\tau) \rangle}{\langle P \rangle^2} \quad (1)$$

where $< >$ stands for ensemble average, while the RIN is given by the Fourier transform of $C_{PP}(\tau)$ [47, 48].

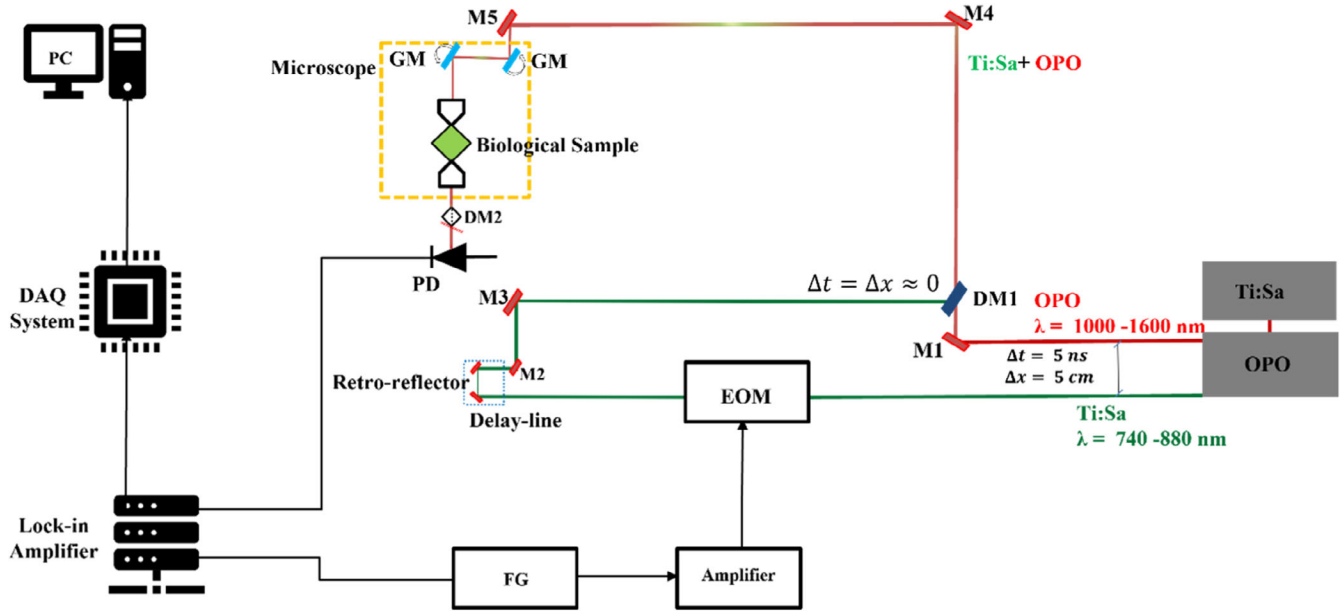

FIGURE 1 Schematic representation of optical architecture of SRS microscope. DAQ, data acquisition system; DM1, DM2, dichroic mirror; EOM, electro-optic modulator; FG, function generator; GM, galvo mirror; M1 to M5, mirror; PC, personal computer; PD, photodiode; OPO, optical parametric oscillator; Ti:Sa, Ti:Sapphire laser

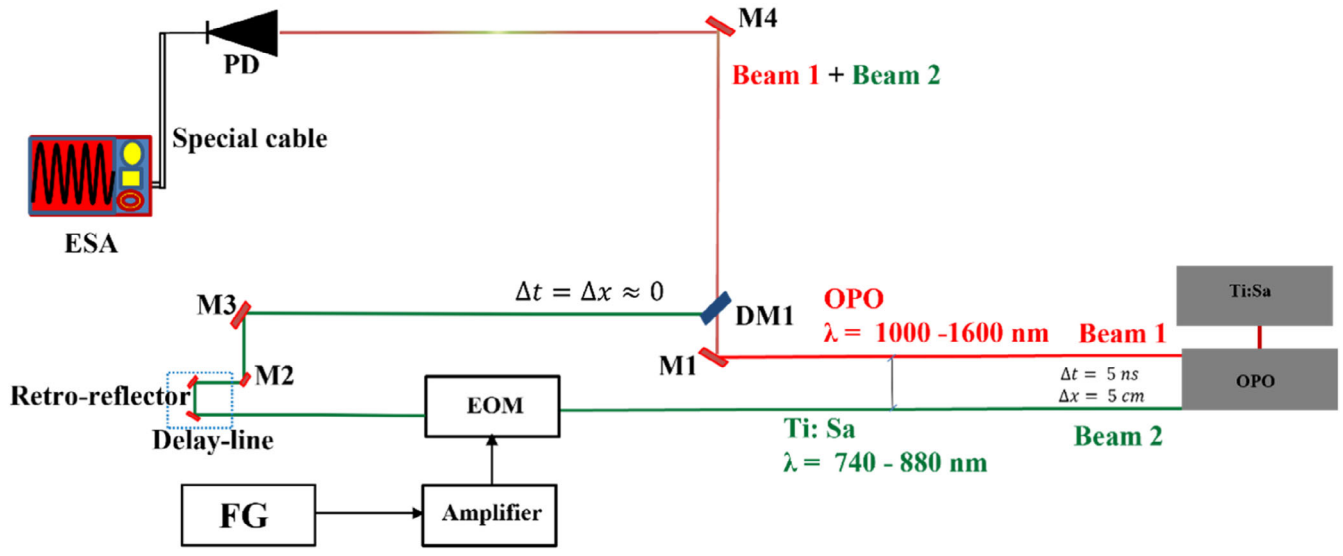

FIGURE 2 Optical architecture for RIN measurement. DM1, dichroic mirror; ESA, electronics spectrum analyzer; EOM, electro-optic modulator; FG, function generator; M1 to M4, mirrors; PD, photodiode; OPO, optical parametric oscillator; Ti:Sa, Ti:Sapphire laser

To measure the RIN of both Ti:Sa and OPO sources, a fast photodiode is placed after the mirror M4 in Figure 2. The laser radiation is focused in the active area of the photodiode, and the latter is linked to an RFS analyzer (Rohde & Schwarz FS300) through a special cable (CBL-4FT-SMSMT) to avoid external disturbances.

2.2 | Noise measurements in the detection system

The noise power at the PD output is determined by the contribution of three mutually statistical independent noise sources: the thermal noise, the shot noise and the excess noise [2]:

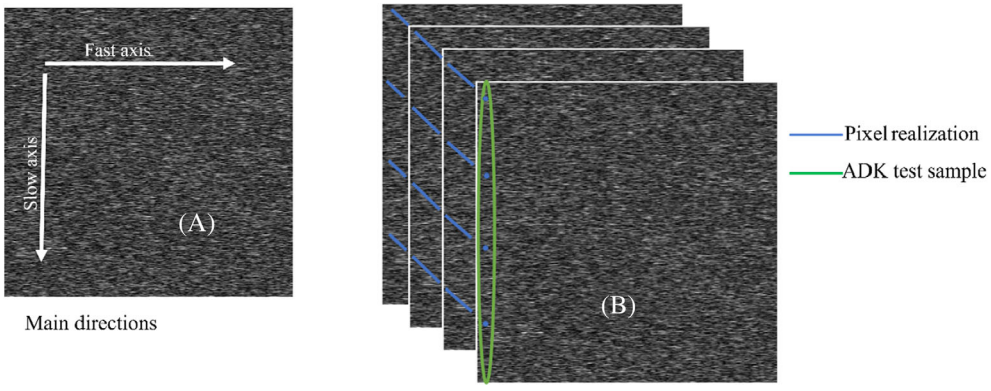

FIGURE 3 Image test directions: (A) The main direction for the Ljung-Box Q-test (LBQ) test (B) Anderson-Darling k-sample test along with slow axis

$$V_{\text{Noise}} = \sqrt{V^2_{\text{Johnson}} + V^2_{\text{Shot noise}} + V^2_{1/f}} \tag{2}$$

Johnson noise is given by:

$$V_{\text{Johnson}} = \sqrt{4K_B TR\Delta f} = \sqrt{\frac{2K_B TR}{\Delta t}} \tag{3}$$

Here, K_B is the Boltzmann constant, Δf is the measurement bandwidth in Hz given by $\Delta f = 1/(2\Delta t)$, where Δt is the signal-collection time constant, that is, the LIA integration time in our case, T is the absolute temperature in Kelvin degree (typically 300 K) and R is the load resistance in ohms. The power in thermal noise is proportional to the square of V_{Johnson}, which is independent of frequency for a fixed bandwidth (white noise).

In a PD, the shot noise is given by the statistical fluctuations in both the photocurrent (i_P) and the detector dark current (i_D), which satisfy the following equation:

$$V_{\text{Shot noise}} = \sqrt{2e(i_p + i_D)\Delta f}.R = \sqrt{\frac{e(i_p + i_D)}{\Delta t}}.R \tag{4}$$

where e is the elementary charge, $i_P = \hat{R}$*P is the photocurrent, $\hat{R}$ is the responsivity [A/W] of the detector, P is the average light power detected by the PD, i_D is the detector dark current; typically, i_D is much weaker than i_P. For a fixed bandwidth, the noise current is independent of frequency (white noise).

In the SRS technique, a small alternative voltage (AC) at the sub-microvolt level from a noisy environment has to be extracted. Due to their phase-sensitive detection, LIAs, with their high sensitivity and SNR, are suitable for this scope. A LIA is essentially a bandpass amplifier with variable central frequency and bandwidth, allowing significant improvement in noise rejection.

We note that when a noise voltage is measured, the observed value is dependent on the bandwidth of the measuring instrument unless a filter is used to limit the bandwidth. In this case, a filter's equivalent noise bandwidth (ENBW) must be defined. In a LIA, the ENBW is determined by the LIA time constant (τ_{LIA}) and slope; for a slope of 18 dB/octave, the ENBW of a time constant τ_{LIA} is given by $3/(32\tau_{LIA})$. In our LIA, the typical input noise is 2 nV/√Hz (typical), with a maximum value of 4 nV/√Hz.

2.3 | Statistical properties analysis of image noise and imaging processing

In order to analyze the statistical properties of image noise, acquisitions of background noise images as a function of the power incident onto the PD were carried out in the range from 1.5 to 13.5 mW with a step of 1 mW. For each fixed power level, a set of 10 images were acquired.

Statistical properties analysis of image noise was carried out for each set of fixed power levels. In order to verify the hypothesis of uncorrelation (necessary for independence), the unidimensional Ljung-Box Q-test (LBQ) test [49, 50] was applied on both the fast axis and slow axis (see Figure 3A) of each image ($k = 1, ..., 10$). In order to accept the hypothesis of uncorrelation for the considered directions (fast axis and slow axis), the percentage of confirmation was fixed at 95%.

The Anderson-Darling k-samples test (ADK test) [51] was used to verify the hypothesis of identical distribution for each set of fixed power levels. Because the ADK test is bidimensional and the hypothesis of uncorrelation was accepted along the low axis, we individuate 512 matrices with dimensions [10, 512] to perform the ADK test. Each matrix was obtained by putting together the columns with the same index for all the k images of the set ($k = 1, ..., 10$; see Figure 3B). Also, in this case, the hypothesis of identical distribution was accepted if the percentage of confirmation was 95%.

As image quality metric, in this article, SNR is used, which is given by the ratio of the mean signal value of foreground to the standard deviation of the background:

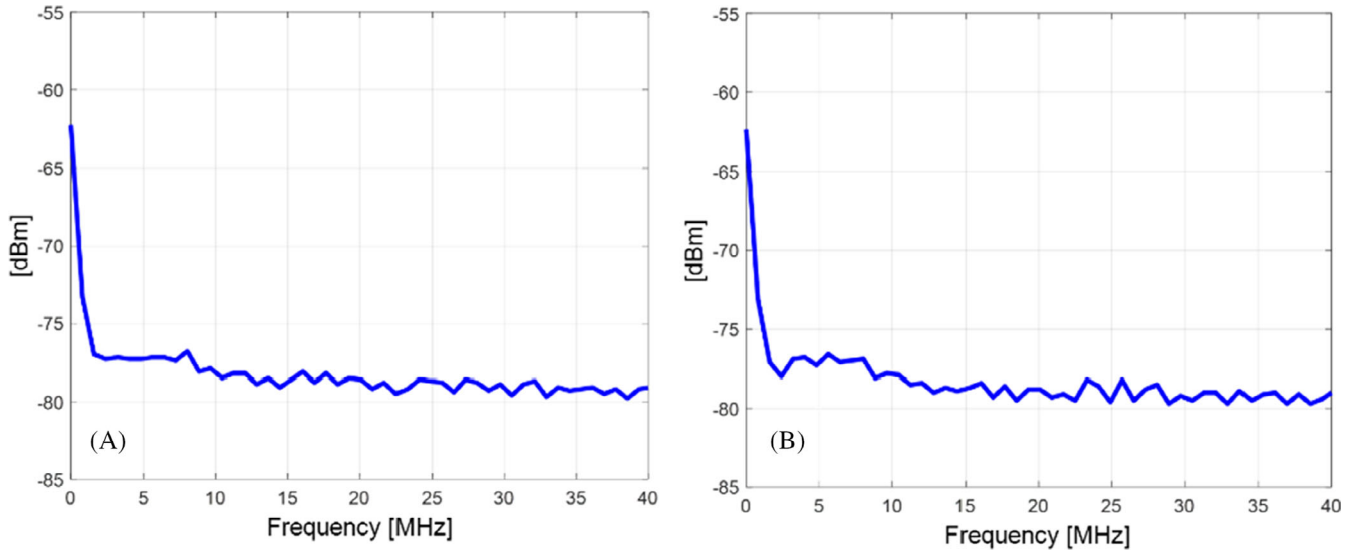

FIGURE 4 RIN measurements for laser: (A) Ti:Sa at $\lambda = 808$ nm and (B) OPO at $\lambda = 1075$ nm

$$SNR = \frac{\text{Mean}(\text{foreground})}{\text{SD}(\text{background})} \tag{5}$$

The procedure to calculate the SNR is the following: (1) a mask is manually created Supporting Information (S1); (2) the foreground is individuated by an element-wise multiplication of the mask with the original image and its average value is calculated; (3) the background is individuated by an element-wise multiplication of (1 − mask) with the original image and its standard deviation is computed; (4) the SNR is estimated.

We defined the Relative SNR increment (RSNRI) as:

$$RSNRI(A_i) = \frac{SNR_f(A_i) - SNR_b}{SNR_b} \tag{6}$$

where $SNR_f(A_i)$ is the SNR evaluated after filtering with the denoising algorithm A_i, while SNR_b is the SNR value before applying A_i. Taking advantage of RSNRI, in this article, the performances of SVD, DWT and SSA have been compared with the aim to assess the differences among different methods in noise reduction Supporting Information (S1).

3 | RESULTS AND DISCUSSION

It is recognized that laser noise in SRS is an important parameter, and that modulation must be carried out at frequencies slightly higher than the flattening of the RIN curve. RIN measurements of Ti:Sa at $\lambda = 810$ nm and OPO at $\lambda = 1053$ nm (which correspond to a Raman shift of 2845 cm^{-1}) are reported in Figure 4A,B.

As it can be seen in Figure 4A,B, in our SRS spectroscopy experimental set up the shot noise regime is achieved for both Ti:Sa and OPO sources around the fixed modulation frequency (5 MHz).

To investigate the noise in our SRS detection system, the noise levels of the LIA voltage were measured when Ti:Sa pulses were blocked while only OPO pulses were impinged on the PD. We assigned the wavelength of 1053 nm to OPO while its optical power was gradually increasing and divided into 10 steps. Lock-in measurements were acquired in the group of 10 for each power value. The acquisition time of each measurement was 16 s. The LIA time constant was set to 100 μs with an 18 dB/oct slope and sensitivity of 10 μV. Data were processed and the standard deviation normalized to the square root of bandwidth (30.6 $\sqrt{Hz}$) and to the gain of lock-in (10^6) are shown in Figure 5.

However, we can see in Figure 5, in which Johnson noise (Equation 3) and the shot noise (Equation 4) at the PD, are plotted, when the laser power is less than of about 2.5 mW the Johnson noise is dominant, while increasing the laser power, the shot-noise becomes dominant with respect to the thermal noise. Therefore, in the range of laser power from 3.5 to 13.5 mW, our SRS system is shot noise limited. In addition, we note a slight discrepancy between theoretical points, given by $(V^2_{Johnson} + V^2_{Shot\ noise})^{1/2}$, and experimental results. Since good low noise amplifiers have an input noise of about 3 nV/√Hz [52], in order to justify this discrepancy, a reasonable option is that it is due to the input noise of LIA.

To investigate the statistical properties analysis of image noise, we acquired background noise images in

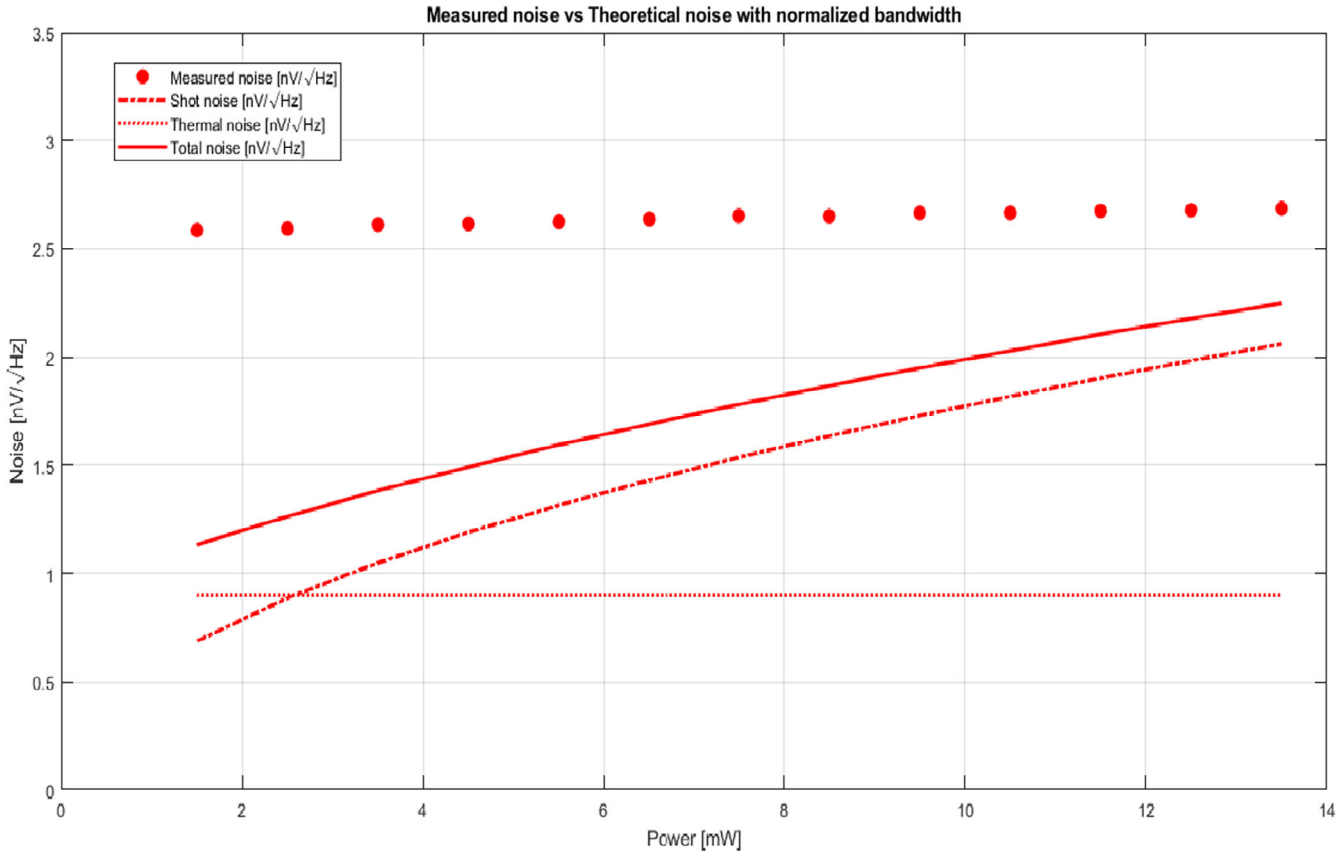

FIGURE 5 Measured and calculated noise when laser power is in increasing order from 1.5 to 13.5 mW with the steps of 1 mW

TABLE 1 Ljung-Box *Q*-test results for different incident power

Percentage of uncorrelated arrays													
Power (mW)	1.5	2.5	3.5	4.5	5.5	6.5	7.5	8.5	9.5	10.5	11.5	12.5	13.5
Fast axis (%)	0.2	0.2	0.2	0.2	0.2	0.2	0.2	0.2	0.2	0.2	0.2	0.2	0.2
Slow axis (%)	98.9	98.6	98.5	98.9	98.8	98.6	99	98.6	99.2	99.3	99.1	99.1	98.8

groups of 10, increasing the power from 1.5 to 13.5 mW with an interval of 1 mW, as described in Section 2.3. All the images were the single recording of 512 px × 512 px, and their acquisition times were 16 s. The LIA time constant was set to 100 μs with an 18 dB/oct slope and a sensitivity of 10 μV. The results from the LBQ tests are reported in Table 1. The tests were carried with a 1% significance level to increase the test power. The percentage of uncorrelated columns was ≈99% for each incident power, while the percentage of uncorrelated rows was always 0.2% for each incident power. Therefore, the uncorrelation hypothesis was accepted along the slow axis and rejected along the fast axis for every incident power.

The LBQ analysis reveals an interesting noise correlation along the fast axis. It can be explained considering that the time constant of the LIA (100 μs is about 3× the pixel dwell time (30 μs). Therefore, fluctuations are expected to be correlated over a few pixels along this direction. On the contrary, along the slow axis, a correlation is not expected because the time gaps between the pixels (given by about 516× pixel dwell time) are significantly greater than the time constant of the LIA. In Figure 6, the noise correlations between adjacent pixels along the fast axis are reported and a correlation among three consecutive pixels is demonstrates.

Our result confirms the general rule according to which, in order to distinguish fluctuation from one pixel to the next, the lock-in bandwidth should match the pixel acquisition rate. However, because this matching condition is not made explicit in many articles, we guess it is not achievable in all the SRS microscopes presented in literature, so the statistical properties analysis of images

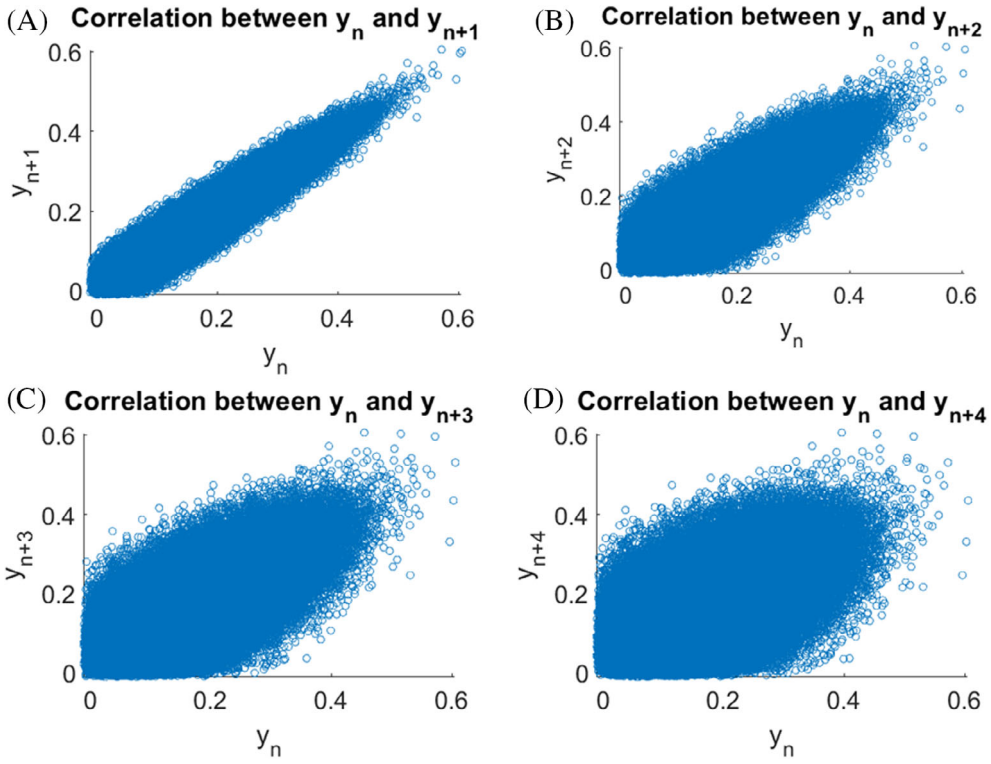

FIGURE 6 Correlation between two pixels along the fast axis: the correlation between two pixels along the fast axis of Figure 3A is evaluated using scatter plots. From (A) to (D): the scatter plot between y_n (n-th pixel) and $(y_{n+k}$ $(n+k)$-th pixel, $k=1,2,3,4))$ reveals a strong linear correlation between adjacent pixels, which slowly drops to zero approximately after 3 pixels

TABLE 2 Anderson-Darling k-sample test results for different incident power

Percentage of columns in which pixel resulted from the same distribution													
Power (mW)	1.5	2.5	3.5	4.5	5.5	6.5	7.5	8.5	9.5	10.5	11.5	12.5	13.5
Slow axis (%)	99	99.2	98	98	100	97.1	99.2	98.8	100	98.2	97.9	99.2	98.4

noise represents an important step toward optimization of SRS images denoising.

The results of ADK tests are reported in Table 2. The tests were carried with a 1% significance level. The percentage of columns in which pixels can be considered as extracted from the same distribution was in the range [97%, 100%] for every incident power. The background noise can definitely be considered an identically distributed white noise along with columns, while it is correlated along rows for every incident power.

The image processing analysis was performed on several SRS images of lipid droplets (LDs) inside adipocyte cells. For investigation of the C—H_2 bond of lipids—having a Raman shift of 2845 cm^{-1}—our pump signal was set to 810 nm and Stokes signal at 1053 nm. For all samples, the power of the pump and Stokes incident onto the sample was set to 11 mW. The LIA time constant was fixed to 100 μs with an 18 dB/oct slope and a sensitivity of 10 μV. Each SRS acquired image is a single collection of 512px × 512px, and the acquisition time was 16 s.

In Figure 7, in the top line, on the left an example of raw SRS image (A) and on the right the images obtained denoising the raw image by DWT (B) are, respectively, reported. In the bottom line, the images obtained denoising the raw image by SVD (C) and by SSA (D) are reported on the left and on the right, respectively.

The RSNRI distributions given by each denoising method are shown in Figure 8. For each method, in each boxplot the black dots represent different images used to build the box, while the red dot indicates the RSNRI average value.

The red line indicates the median on each box, and the bottom and top edges of the box indicate the 25th and 75th percentiles, respectively.

As we can see in Figure 8, SSA exhibits a higher median for RSNRI when compared to both SVD and DWT method, which means a higher SNR increment. In order to justify the improvement in image denoising achieved by SSA, we note that the applications of SVD, DWT and SSA are based on the hypothesis of white noises. On the contrary, we have demonstrated a noise correlation along the fast axis, therefore, being SSA one-dimensional algorithms, it has been applied along the slow axis.

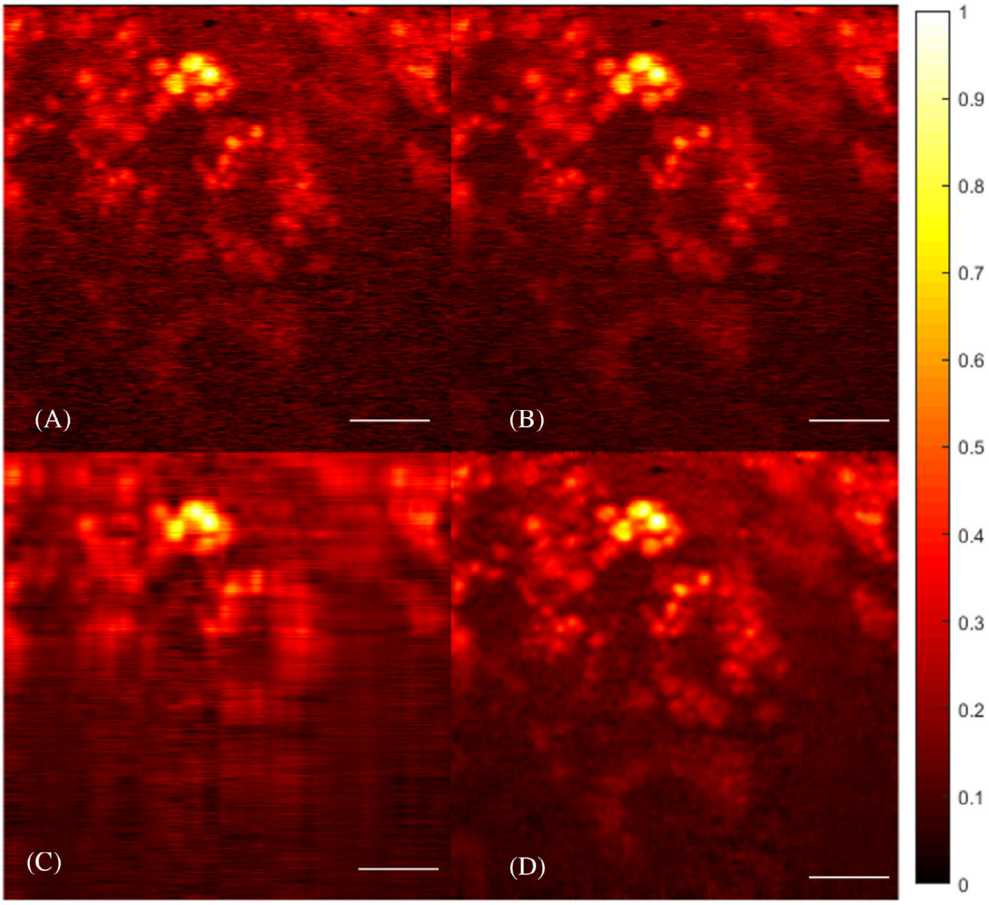

FIGURE 7 Comparison of raw image (A) and images processed by discrete wavelet transform (DWT) (B), singular value decomposition (SVD) (C) and singular spectrum analysis (SSA) (D) for lipid droplets; Scale bar = 10 μm

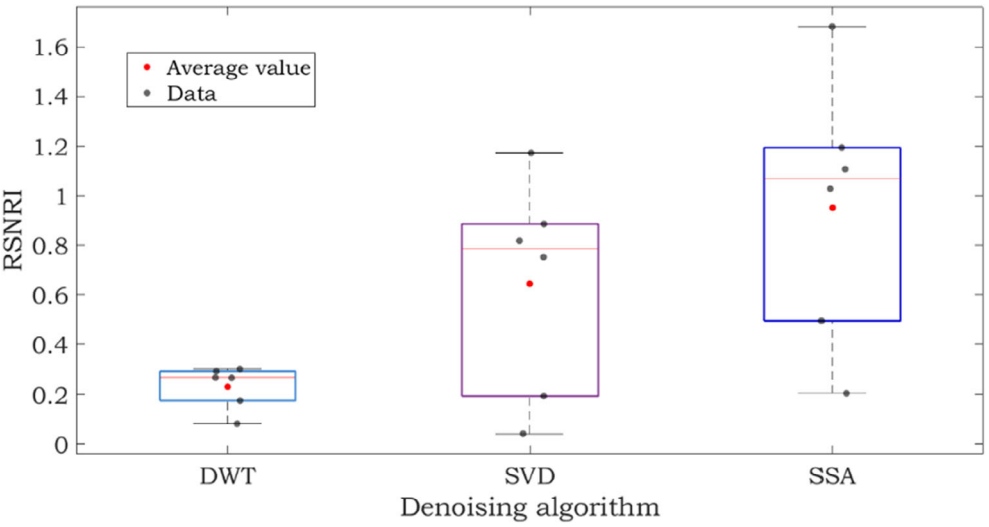

FIGURE 8 Boxplot of relative SNR increment (RSNRI) given by various denoising methods

An interesting aspect is the capability of the different denoisers to resolve the edges of the lipids. A qualitative evaluation can be obtained from Figure 9, in which on the left column, a slice is reported on each SRS denoised image, while on the right column, for each used algorithm, the signals along the slice of both raw image and filtered one are reported.

A quantitative evaluation of the capability of the different denoiser to resolve the edges of the lipids has been obtained calculating the contrast [53] of different SRS images. They have been compared by using relative contrast increment (RCI), which was defined in the same way of RSNRI. The results of RCI are shown in Figure 10.

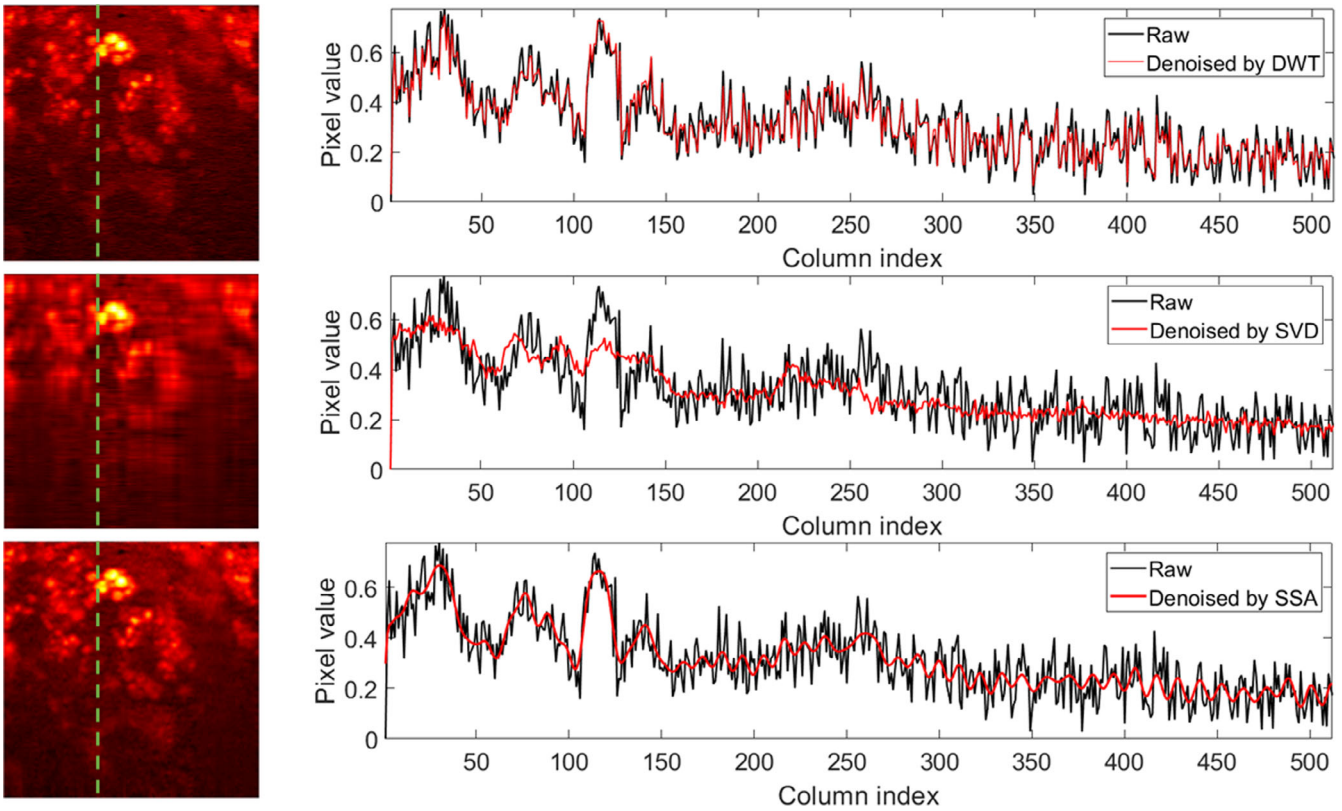

FIGURE 9 Qualitative evaluation to preserve edges. In the right column: *on the top*, the signal of raw image is compared with the one of image obtained filtering by discrete wavelet transform (DWT); *in the middle*, the signal of raw image is compared with the one of image obtained filtering by singular value decomposition (SVD); *on the bottom*, the signal of raw image is compared with the one of image obtained filtering by SVD

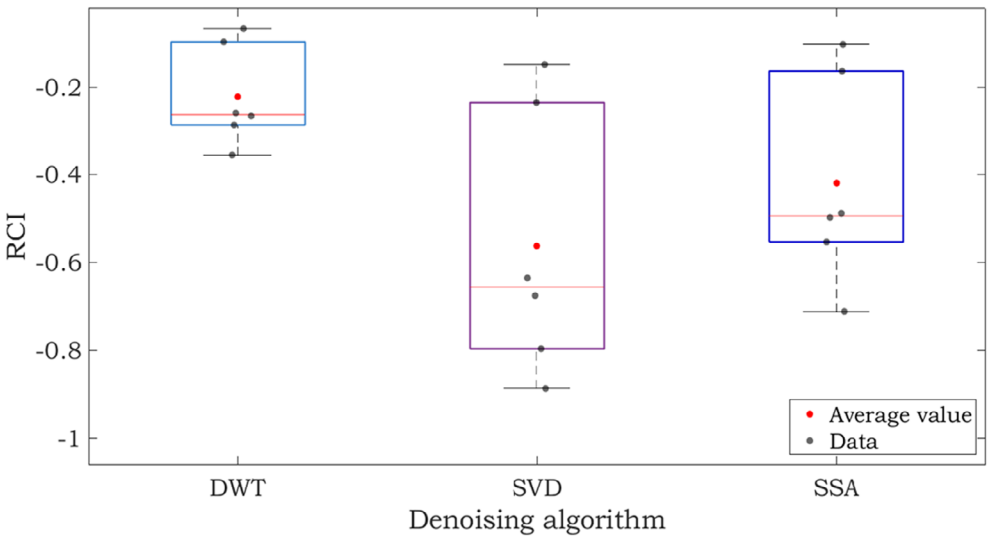

FIGURE 10 Boxplot of relative contrast increment (RCI) given by the examined denoising methods

As confirmed qualitatively by the plots in Figure 9 and quantitatively by relative contrast increment reported in Figure 10, in SRS image denoised by DWT the edges are well preserved, on the contrary, in image denoised by SVD the edges are scarcely preserved, while an acceptable preservation of edges was achieved by SSA.

We presume that correlated noise can affect the edges of SRS images, so dimensions of object along the fast axis can be altered. This could be a problem when a

quantitative evaluation of object size is required. From Figure 10, we obtain that all the algorithms provide an average contrast decrement, so as a preliminary result we can conclude that the used algorithms do not suppress correlated noise.

4 | CONCLUSIONS

This article reports a detailed investigation of the contributions of various types of noises due to the femtoseconds laser, electronics and imaging systems. Measurements on laser noise prove that our lasers system is shot noise limited at higher frequencies (5 MHz). So, our outcome of measures and data analysis confirms that the used sources are well suitable and satisfy our purpose. Measurements noise as a function of laser power demonstrate that our spectroscopic experimental setup is shot noise limited and the measured noise of detection systems is about 3 nV/√Hz, demonstrating that our device represents a *state-of-the-art* tool (a good low noise amplifier will have about 3 nV/√Hz of input noise).

As far as imaging system is concerned, the results of statistical properties of images noise demonstrate a noise correlation along the fast axis. An appropriate setting of lock-in time constant, in principle, could avoid it, but in practical implementations, this is not always possible. So statistical properties analysis of image noise represents a fundamental step in adapting denoising algorithms to signal images.

Taking into account the results obtained from statistical properties analysis, SSA has been applied for SRS imaging. Finally, SVD, DWT and SSA image processing performances have been compared. The adapted SSA algorithm showed a noise reduction with acceptable preservation of edges. We believe that our findings could be generalizable to the variety of nonlinear microscopes readers may use, and they could provide a widely usable methodology to improve biological imaging quality. However, the main merit is that the advantages in terms of complexity reduction in SRS system implementations are of considerable importance for some classes of biological experiments, for example, in vivo-imaging and for increasing SRS microscopy throughput. Definitely, the development of simple, efficient and high accuracy denoising methods can provide an essential perspective for increasing the diffusion of SRS microscopy and the number of its applications.

ACKNOWLEDGMENTS

Open Access Funding provided by Consiglio Nazionale delle Ricerche within the CRUI–CARE Agreement.

CONFLICT OF INTEREST

The authors declare no conflicts of interest.

DATA AVAILABILITY STATEMENT

The datasets generated during and/or analyzed during the current study are available from the corresponding author on reasonable request.

ORCID

Rajeev Ranjan https://orcid.org/0000-0002-4131-6656

REFERENCES

[1] O. Svelto, D. C. Hanna, *Principles of Lasers*, Springer, New York, NY **2010**.
[2] S. Donati, *Photodetectors: Devices, Circuits and Applications*, 2nd ed., Wiley-IEEE Press, Hoboken, NJ **2000**.
[3] M. Flower (Ed.), *Webb's Physics of Medical Imaging*, 2nd ed., CRC Press, Boca Raton **2012**. https://doi.org/10.1201/b12218.
[4] R. C. Gonzalez, R. E. Woods, *Digital Image Processing*, 2nd ed., Prentice-Hall, Inc, Upper Saddle River, NJ **2002**.
[5] M. Sonka, V. Hlavac, R. Boyle, *Image Processing, Analysis and Machine Vision*, 4th ed., Cengage Learning, Boston, MA **2015**.
[6] B. Z. Haq, J. B. Chowdhry, *Eur. Biophys. J.* **1997**, *26*, 419.
[7] S. K. Mohideen, S. A. Perumal, M. M. Sathik, *Int. J. Netw. Secur.* **2008**, *8*, 213.
[8] P. Pradhan, S. Guo, O. Ryabchykov, J. Popp, T. Bocklitz, *J. Biophotonics* **2020**, *13*, e201960186.
[9] Y. R. Shen, N. Bloembergen, *Phys. Rev.* **1965**, *137*, A1787.
[10] N. Bloembergen, *Am. J. Phys.* **1967**, *35*, 989.
[11] J. X. Cheng, X. S. Xie (Eds), *Coherent Raman Scattering Microscopy*, CRC Press, Boca Raton **2012**. https://doi.org/10.1201/b12907.
[12] R. C. Prince, R. R. Frontiera, E. O. Potma, *Chem. Rev.* **2017**, *117*(7), 5070. https://doi.org/10.1021/acs.chemrev.6b00545.
[13] L. Sirleto, M. A. Ferrara, T. Nikitin, S. Novikov, L. Khriachtchev, *Nat. Commun.* **2012**, *3*, 1. https://doi.org/10.1038/ncomms2188.
[14] L. Sirleto, A. Vergara, M. A. Ferrara, *Adv. Opt. Photon.* **2017**, *9*, 169.
[15] M. A. Ferrara, L. Sirleto, G. Nicotra, C. Spinella, I. Rendina, *Photonics Nanostruct.: Fundam. Appl.* **2011**, *9*, 1.
[16] L. Sirleto, A. Aronne, M. Gioffrè, E. Fanelli, G. C. Righini, P. Pernice, A. Vergara, *Opt. Mater.* **2013**, *36*, 408. https://doi.org/10.1016/j.optmat.2013.10.001.
[17] A. M. Streets, A. Li, T. Chen, Y. Huang, *Anal. Chem.* **2014**, *86*, 8506. https://doi.org/10.1021/ac5013706.
[18] J. X. Cheng, X. S. Xie, *Science* **2015**, *350*(6264), aaa8870. https://doi.org/10.1126/science.aaa8870.
[19] C. H. Camp Jr., M. T. Cicerone, *Nat. Photonics* **2015**, *9*(5), 295. https://doi.org/10.1038/nphoton.2015.60.
[20] C. Zhang, D. Zhang, J.-X. Cheng, *Annu. Rev. Biomed. Eng.* **2015**, *17*, 415.
[21] A. Owyoung, *Opt. Lett.* **1978**, *2*(4), 91.
[22] J. P. Heritage, D. L. Allara, *Chem. Phys. Lett.* **1980**, *74*(3), 507.
[23] B. F. Levine, C. V. Shank, J. P. Heritage, *IEEE J. Quantum. Electron.* **1979**, *QE-15*, 1418.
[24] A. Owyoung, *IEEE J. Quantum. Electron.* **1978**, *QE-14*, 192.

[25] D. Dietze, R. Mathies, *ChemPhysChem* **2016**, *17*, 1224.
[26] G. Batignani, C. Ferrante, T. Scopigno, *J. Phys. Chem. Lett.* **2020**, *11*, 7805.
[27] Y. Ozeki, F. Dake, S. Kajiyama, K. Fukui, K. Itoh, *Opt. Express* **2009**, *17*, 3651.
[28] Y. Ozeki, Y. Kitagawa, K. Sumimura, N. Nishizawa, W. Umemura, S. S. Kajiyama, K. Fukui, K. Itoh, *Opt. Express* **2010**, *18*, 13708.
[29] X. Audier, S. Heuke, P. Volz, I. Rimke, H. Rigneault, *APL Photonics* **2020**, *5*, 011101. https://doi.org/10.1063/1.5129212.
[30] M. J. B. Moester, F. Ariese, J. F. de Boer, *J. Eur. Opt. Soc.: Rapid Publ.* **2015**, *10*, 15022.
[31] K. Nose, Y. Ozeki, T. Kishi, K. Sumimura, N. Nishizawa, K. Fukui, Y. Kanematsu, K. Itoh, *Opt. Express* **2012**, *20*(13), 13958. https://doi.org/10.1364/OE.20.013958.
[32] L. Zada, B. Fokker, H. A. Leslie, A. D. Vethaak, J. F. de Boer, F. Ariese, *J. Eur. Opt. Soc.: Rapid Publ.* **2021**, *17*, 10. https://doi.org/10.1186/s41476-021-00155-w.
[33] C. S. Liao, J. H. Choi, D. Zhang, S. H. Chan, J. X. Cheng, *J. Phys. Chem. C* **2015**, *119*, 19397.
[34] Y. Li, B. Shen, G. Zou, S. Wang, Q. Junle, R. Hu, L. Liu, *J. Biophotonics* **2021**, *14*(8), e202100080. https://doi.org/10.1002/jbio.202100080.
[35] B. Manifold, E. Thomas, A. T. Francis, A. H. Hill, F. Dan, *Biomed. Opt. Express* **2019**, *10*(8), 3860. https://doi.org/10.1364/BOE.10.003860.
[36] P. Abdolghader, A. Ridsdale, T. Grammatikopoulos, G. Resch, F. Légaré, A. Stolow, A. F. Pegoraro, I. Tamblyn, *Opt. Express* **2021**, *29*(21), 34205. https://doi.org/10.1364/OE.439662.
[37] H. Lin, H. J. Lee, N. Tague, J. B. Lugagne, C. Zong, F. Deng, J. Shin, L. Tian, W. Wong, M. J. Dunlop, J. X. Cheng, *Nat. Commun.* **2021**, *12*, 3052. https://doi.org/10.1038/s41467-021-23202-z.
[38] N. Golyandina, V. Nekrutkin, A. Zhigljavsky, *Analysis of Time Series Structure: SSA and Related Techniques*, Chapman & Hall, New York, NY **2001**.
[39] A. M. Tomé, D. Malafaia, A. R. Teixeira, E. W. Lang, On the use of singular spectrum analysis. *arXiv:1807.10679* **2018**, 1.
[40] A. D'Arco, N. Brancati, M. A. Ferrara, M. Indolfi, M. Frucci, L. Sirleto, *Opt. Express* **2016**, *7*(5), 1853. https://doi.org/10.1364/BOE.7.001853.
[41] A. D'Arco, M. A. Ferrara, M. Indolfi, V. Tufano, L. Sirleto, *J. Nonlinear Opt. Phys. Mater.* **2017**, *26*(4), 1750052. https://doi.org/10.1142/S0218863517500527.
[42] R. Ranjan, A. D'Arco, M. A. Ferrara, M. Indolfi, M. Larobina, L. Sirleto, *Opt. Exp.* **2018**, *26*(20), 26317.
[43] R. Ranjan, M. Indolfi, M. A. Ferrara, L. Sirleto, *J. Vis. Exp.* **2019**, (149), e59614. https://doi.org/10.3791/59614.
[44] M. A. Ferrara, A. Filograna, R. Ranjan, D. Corda, C. Valente, L. Sirleto, *PLoS ONE* **2019**, *14*(5), e0216811. https://doi.org/10.1371/journal.pone.0216811.
[45] R. Ranjan, M. A. Ferrara, A. Filograna, C. Valente, L. Sirleto, *J. Instrum.* **2019**, *14*, P09008. https://doi.org/10.1088/1748-0221/14/09/P09008.
[46] L. Sirleto, R. Ranjan, M. A. Ferrara, *Appl. Sci.* **2021**, *11*, 3903. https://doi.org/10.3390/app11093903.
[47] J. Kim, Y. Song, *Adv. Opt. Photonics* **2016**, *8*(3), 465. https://doi.org/10.1364/AOP.8.000465.
[48] D. von der Linde, *Appl. Phys. B* **1986**, *39*, 201.
[49] G. E. P. Box, G. M. Jenkins, *Time Series Analysis: Forecasting and Control*, Holden-Day, San Francisco, CA **1970**.
[50] G. M. Ljung, G. E. P. Box, *Biometrika* **1978**, *65*(2), 297.
[51] F. W. Scholz, M. A. Stephens, *K-sample Anderson-Darling tests of fit, for continuous and discrete cases, Technical Report, No. 81*, May 1986, Department of Statistics GN-22, University of Washington, Seattle, WA **1927**.
[52] *Lock-in Amplifier Model SR844 RF Stanford Research Systems*. User's Manual
[53] Q. Wu, F. A. Merchant, K. R. Castleman, (Eds,). *Microscope Image Processing*, Elsevier-Academic Press, Cambridge, MA **2008**. https://doi.org/10.1016/B978-0-12-372578-3.00001-5.

SUPPORTING INFORMATION

Additional supporting information may be found in the online version of the article at the publisher's website.

How to cite this article: R. Ranjan, G. Costa, M. A. Ferrara, M. Sansone, L. Sirleto, *J. Biophotonics* **2022**, *15*(6), e202100379. https://doi.org/10.1002/jbio.202100379